Dynamics of impacting a bubble by another pulsed-laser-induced bubble: Jetting, fragmentation, and entanglement

Yen-Hung Chen and Lin I

Department of Physics and Center for Complex Systems, National Central University, Chungli, Taiwan 32054, Republic of China

(Received 26 May 2007; revised manuscript received 18 December 2007; published 13 February 2008)

We investigate experimentally the detailed dynamics of how an existing microbubble B_1 is impacted and shattered by another nearby pulsed-laser-induced microbubble B_2, and the backward interaction on B_2 in a thin liquid layer. Mediated by the flow field, potential energy can be accumulated or lost through the alternate compression and expansion of the two bubbles. The symmetry breaking induced by the presence of the nearby counterbubble generates push-pull-type alternate forward and backward axial jetting on the compressed bubble associated with the elongated shape or even entrainment of the counterexpanding bubble into the jet-indented boundary. The strong penetrating axial jet through B_1, and its interplay with the transverse jets by the flow field surrounding B_1 in the first compression stage and the second expanding stage of B_1 lead to a complicated fragmentation pattern of B_1. Increasing the interbubble interaction by decreasing the interbubble distance causes B_2 to become entangled with B_1 through its entrainments into the backward axial jet-indented region of B_2, in the expansion phase of B_2. At the extreme of large laser energy for B_2, the leftward reexpansion of B_1 is suppressed. The strong shear flow field generates many tiny bubbles around the liquid-gas boundaries of the two axial jet-induced major daughter bubbles from B_1. The detailed interaction behaviors over a broad range of the energy of B_2, 0.14–0.55 μJ (corresponding to the maximum bubble expansion energy), and of the interbubble distance (170–500 μm) are presented and discussed.

DOI: 10.1103/PhysRevE.77.026304 PACS number(s): 47.55.dp, 47.20.Ma

I. INTRODUCTION

Bubble phenomena are ubiquitous in our daily life. The dynamics of bubble generation, expansion, collapse, and interaction are interesting nonlinear problems [1]. In liquids, cavitation bubbles can be formed under sudden tensile stress or under sudden deposition of energy. The cavitation bubbles generated by a rotating propeller, ultrasonic drive [2,3], or focused laser pulses are a few good examples [4,5]. A collapsing bubble leads to interesting phenomena such as sonoluminescence [6,7] and pressure wave emission [8,9]. The jet formation associated with the collapsing bubble generated by a shrimp claw is responsible for predation in the ocean [10,11]. The interaction of cavitation bubbles has also attracted attention in many medical applications and fundamental research [12].

If the background symmetry is broken, a bubble no longer expands and collapses isotropically. The anisotropic disturbance can be amplified because the surface tension cannot provide a sufficient restoring force on the bubble surface. The jet formation associated with the collapsing bubble near a solid boundary is a well-studied subject [13–16]. The boundary limits the inward flow at the near end, which induces a higher-speed inward flow at the far end. Its nonlinear growth generates a penetrating jet from the far end toward the solid boundary. That is, similarly to the Richtmyer-Meshkov (RM) surface instability across a perturbed interface between high- and low-density fluids, an inertia-dominant instability leads to jet formation [17,18]. This is the source for cavitation erosion on a propeller surface [1]. Ultrasonic cleaning is also based on a similar mechanism associated with the collapsing-microbubble-induced jets. On the other hand, near a free surface, the easier displacement of the free surface induced by the outward flow associated with an expanding bubble also causes the formation of an outward normal jet at the free surface [19,20]. The adjacent expanding bubble is elongated with a pointed pole entrained into the jet. The pressure built up during the overshooting process provides an energy source for the backward jet into the bubble in its subsequent collapse phase.

The system symmetry can also be broken by shock and high-pressure waves generated from external drives, by buoyancy-induced bubble motions, or by hydrodynamic coupling with other bubbles. For example, for a low-density gas bubble surrounded by a soap film in a high-density gas background, a gas jet associated with vortex formation through the RM instability is observed when the bubble interface is impacted by a shock wave [21,22]. For a shock-perturbed bubble in a liquid of high inertia, a liquid jet is formed along the propagation direction of the shock wave [23]. The induced jet from the microbubble has potential applications for microsurgery and drug delivery through a membrane. Recently, the rich phenomena of rising bubbles in liquid and extended media have been studied. For example, intermittency associated with mutual bubble interaction was found in the bubbling process on continuous gas injection into water [24]. In a viscoelastic micellar solution, a rising bubble exhibits oscillatory motion associated with shear thinning and thickening [25].

Pulsed laser microbeams have also been used for cell lysis associated with the outward propagation of a pressure wave from a generated bubble [12]. Multiple microbubbles can easily be generated by successive laser pulses. How a microbubble B_2 generated by the second laser pulse interacts with a nearby existing first bubble B_1 is a complicated and important issue but has been less well studied. In our previous work [26], the mutual interactions between two laser-

TABLE I. Laser energies E_2, distance D_L between the laser pulses for B_1 and B_2, average velocities of jets on B_1, Weber and Reynolds numbers of the jets, and initial expanding velocities of B_2 (the two rightmost columns) for the tested cases from A to J.

Case	E_2 (μJ)	D_L (μm)	V_{jet} (m/s)	We_{jet} (10^3)	Re_{jet} (10^3)	We_{exp} (10^3)	Re_{exp} (10^3)
A	67	500	11	0.1	0.3	2.0	0.7
B	90	500	24	0.6	0.6	5.6	1.2
C	105	500	31	1.1	0.8	8.1	1.5
D	120	500	42	2.0	1.0	11.1	1.7
E	140	500	48	2.6	1.2	13.6	1.9
F	105	350	48	2.6	1.2	8.1	1.5
G	90	300	57	3.7	1.4	5.6	1.2
H	90	225	85	8.2	2.1	5.6	1.2
I	90	170	100	11.4	2.5	5.6	1.2
J	220	225	170	32.8	4.2	22.7	2.5

induced bubbles associated with jetting, fragmentation and entanglement were briefly addressed in a thin liquid layer between two glass slides on a digitally controlled microscope stage through high-speed photography. The precise control of the initial conditions and the high repeatability of the experiment allow the temporal evolution of the interaction to be monitored. A similar method has also been used recently to investigate the pulsed-laser-induced single-bubble dynamics of thin liquids with rigid boundaries in microfluidic devices [16].

In this work, following our earlier work [26], we report the detailed dynamics of the interaction, fragmentation, and entanglement of laser-induced microbubbles, with particular emphasis on the backward interaction, through a more detailed survey of the effects of varying the laser pulse energy E_2 used to generate B_2 and the interbubble distance D_L over broader ranges (see the conditions of tested runs with different combinations of E_2 and D_L in Table I). We first demonstrate how the expansion of B_2 at E_2=90 μJ and D_L =500 μm induces an axial penetrating jet in B_1 in its initial compression stage, and how a butterfly-shaped B_1 can be induced by the two inward transverse jets in its later reexpansion stage. Based on this basic picture, we demonstrate that there is droplet inclusion in B_1 if the B_2-induced axial jet is not strong enough to penetrate B_1 at small E_2, and more complicated fragmentation patterns of B_1 at large E_2. We then address the backward interaction of B_1 on B_2, which induces a pendant-shaped elongation of B_2 entrained in the jet-indented boundary of B_1 initially and then a backward axial jet on B_2 in the compression and expansion stages of B_1, respectively, and how the push-pull-type jetting and entrainment induce entanglement between the two bubbles. We finally address how the entanglement is suppressed and the boundaries of B_1 are shattered into many tiny bubbles, if B_2 is still expanding at the rebound stage of B_1 under very large E_2.

II. EXPERIMENT

The experimental system consists of a liquid cell, a pulse laser system for bubble generation, and a microimaging system as depicted in Fig. 1. A vertical pulsed neodymium-doped yttrium aluminum garnet (Nd:YAG) laser beam (λ =532 nm and 10 ns pulse width) is focused down to 5 μm in diameter on a horizontal thin blue ink layer (water-based inkjet ink, HPI-8449 C, InkTec Co., for Hewlett Packard printers, at 1.25 g/ml density and 0.01 g/cm s viscosity), sandwiched between two horizontal glass slides at 10 μm gap width (capillary coefficient is 22 dyn/cm, contact angle of the ink drop on the glass plate is 5°), through the beam splitter and the objective lens (10× and numerical aperture 0.3) of the microscope (Olympus BX51), to generate the bubble. The laser energy is totally absorbed by the ink solution. The glass slides ($75\times25\times1$ mm^3 for each slide with 60 GPa elastic bending modulus and 4 g/cm^3 density) are separated by stainless steel spacers and mechanically clamped. When B_1 generated by the first laser pulse (laser energy E_1 is fixed at 220 μJ for all the runs in this paper) reaches the final stable state (it can maintain 170 μm in diameter for about 1 min), the digitally controlled microstage with 0.3 μm precision is shifted a distance D_L horizontally for the generation of B_2 by the second laser pulse. Because of the precise controls of the energies E_1 and E_2 and of the distance D_L between the two successive laser pulses, the initial condition of the experiment is highly reproducible (less than 3% fluctuation). By gradually shifting the triggering time of an intensified charged coupled device (ICCD) camera mounted on top of the microscope, the dynamical evolutions of both bubbles after the second laser pulse are studied in detail. A white light emitting diode (LED) mounted below the liquid cell and triggered synchronously with the ICCD

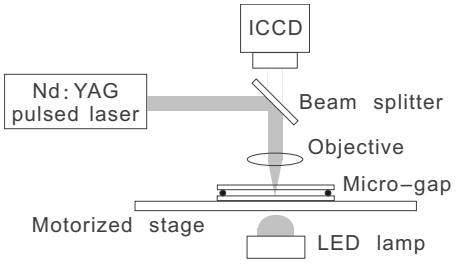

FIG. 1. Side view of the experimental setup.

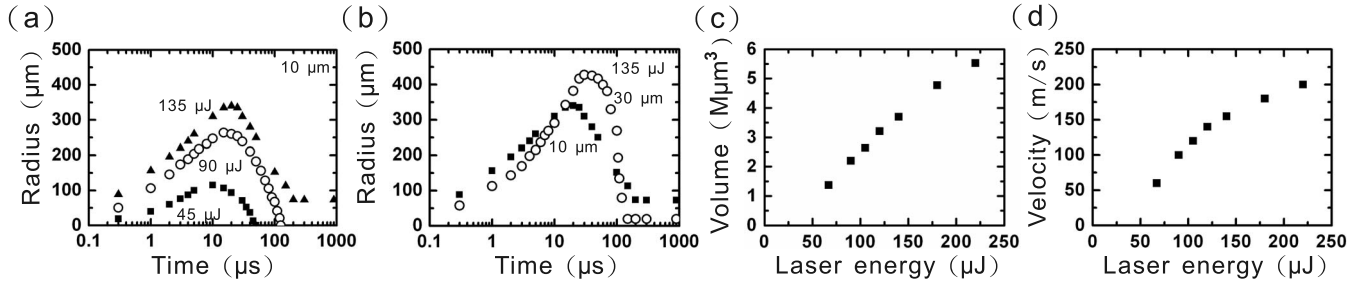

FIG. 2. (a) Radius evolution of the pulsed-laser-induced single bubbles at laser energies of 45 (solid squares), 90 (open circles), and 135 μJ (solid triangles) in the microgap of 10 μm. (b) Radius evolutions at laser energy of 135 μJ, but different gap widths of 10 (solid squares) and 30 μm (open circles). (c) Maximum volumes of the bubble expansion for the different laser energies. (d) Expanding velocities of the bubble boundaries in the initial 1 μs for the different laser energies.

exposure is used for illumination. The exposure time of the ICCD is fixed at 1 μs. Each ICCD trigger allows an immediate exposure and a second exposure after 30 ms. The time evolution of bubbles can be constructed by repeating the runs with the same initial condition. Table I shows the operating parameters with different combinations of E_2 and D_L (at fixed $E_1=220$ μJ) for tested cases A–J in this study.

III. RESULTS AND DISCUSSION

A. Single-bubble evolution

Figure 2(a) depicts the single-bubble radius evolution at the different laser pulse energies. The sudden absorption of laser energy vaporizes the liquid. The hot vapor expands rapidly. After overshooting the surrounding outward liquid flow, the bubble starts to collapse and disappear. At sufficient laser pulse energy, the bubble collapses to a final circular shape. It persists for about 1 min. At 10 μm gap width, the time to reach the maximum volume, t_m, increases from about 10 to 18 μs when the laser pulse energy increases from 45 to 90 μJ, and remains about the same when the laser energy increases further. The bubble takes 35 and 90 μs to collapse at laser energies of 45 and 90 μJ, respectively. The initial expansion has high speed (100 m/s). The maximum bubble volume and the initial expanding velocity of the bubble against the laser energy are shown in Figs. 2(c) and 2(d), respectively. The estimated mechanical energy at the maximum expansion volume is less than 1% of the laser energy according to the method used by Vogel *et al.* [4]. Right after the laser pulse, the Reynolds number ($\rho LU/\mu \sim 1000$) and Weber number ($\rho LU^2/\gamma \sim 5000$) are both high, where L is the gap width, ρ is the liquid density, U is the velocity, μ is the viscosity (=0.01 g/cm s), and γ is the capillary coefficient (=22 dyn/cm). The velocity drops tenfold in the initial 10 μs, while the large values of Reynolds and Weber numbers are still maintained. This indicates that the initial expansion process is dominated by inertia but not by viscosity and surface tension. The boundary layer near the glass plate is about 1 μm in the initial 1 μs and changes to about 3 μm at 10 μs of the expansion process [16]. The thickness of the boundary layer gradually increases with decreasing flow velocity, and eventually spans the whole gap when the bubble expansion is about to reach maximum volume. The clear image of the bubble boundary rules out the possibility of a sharp tonguelike velocity profile. In the later collapsing stage with low bubble boundary speed, the surface tension becomes important, which is evidenced by the evolution toward a spherical-shaped fragmented bubble with increasing time in Fig. 3(a).

The radius evolution at larger gap width (30 μm) is shown in Fig. 2(b) to check the effect of different gap widths. The energy transferred to generate bubbles in both cases (10 and 30 μm) is about the same since the laser energies are both nearly totally absorbed by the liquid (the measurements show that less than 1% is transmitted). The two crossovers of the curves of the two cases indicate that the initial acceleration process is slower, the overshoot process is more obvious, and the collapse process after the slow turnover is faster in the wider gap. This evidences the enhanced inertia effect due to the larger mass of the liquid in the wider gap, which leads to a decrease of relative dissipation, especially in the later stages. Actually, the generic dynamical behaviors of the two-bubble interaction are very similar when the gap width is adjusted. We also check the possible effect of the vertical displacement of the glass slide after the laser pulses. The transverse sound speed in the glass is 2000 m/s and the sound speed in water is 1500 m/s. In the initial 1 μs of the bubble expansion, the pressure wave influences an area ($\sim$1000 μm in radius) much larger than the expanding bubble. Also note that the bending of the glass plate with bending modulus 60 GPa caused by the initial expanding bubble with pressure of a few tens of megapascals [12] is negligible. From the point of view of the inertia effect, the inertia per unit area for the glass is more than 300 times larger than that of the thin liquid. Furthermore, the bubble pressure dramatically drops with growing bubble size. Therefore, the vertical displacement should be less than 1 μm as the bubble expands horizontally to 300 μm in radius. Doubling the slide thickness, which doubles its inertia and the elastic bending force, causes only negligible changes in the dynamical behaviors of bubbles. We therefore fix our gap width at 10 μm throughout the experiment.

B. Forward interaction: Jet formation and fragmentation through butterfly-shaped reexpanding bubbles

In what follows, we demonstrate the dynamical behaviors of forward interaction between the two bubbles. The sequen-

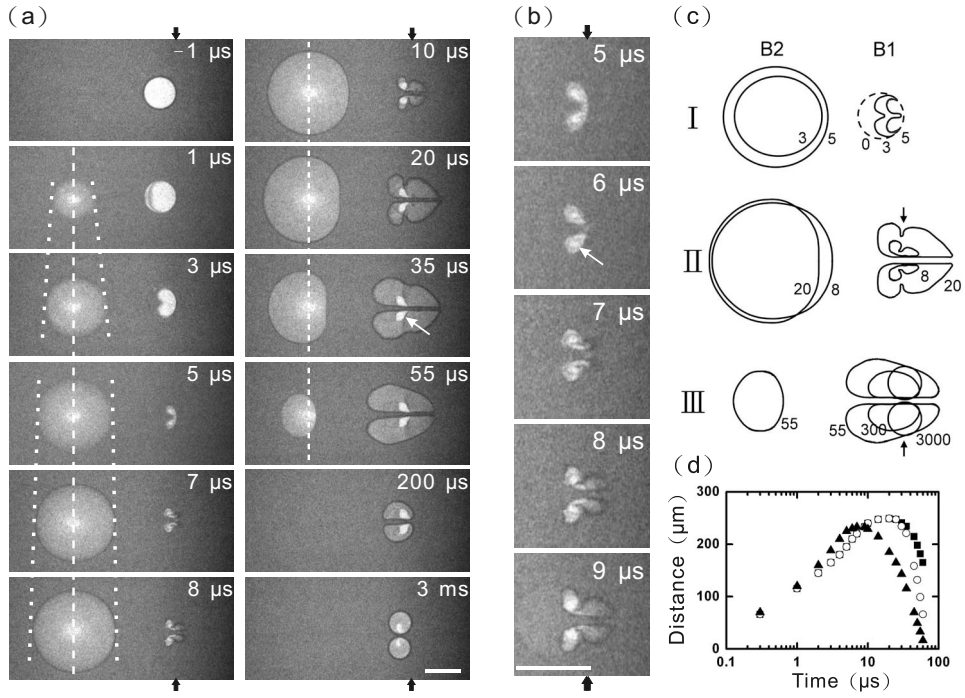

FIG. 3. (a) Sequential snapshots showing the compression, reexpansion, and shrinking of B_1 (the right bubble) with jet formation and fragmentation under the interaction from B_2 (the left bubble) for case B at $E_1=220$ μJ, $E_2=90$ μJ, and $D_L=500$ μm. B_2 is generated at $t=0$ μs. The black arrows indicate the locations of the initial right edge of B_1. The bright areas in B_1 after 8 μs (e.g., the region indicated by the arrow in the panel of 35 μs) correspond to the smallest compressed volume in the entire process, where the two glass surfaces have never been wetted. They allow the best transmission of the illuminating light. The vertical dashed and dotted lines are used as references for the initial horizontal center position of B_2 and the anisotropic expansion from the initial laser position, respectively. (b) Expanded pictures of B_1 from 5 to 9 μs. The white arrows in (a) and (b) indicate the unwetted area and the minimum volume, respectively. Scale bars for (a) and (b) 200 μm. (c) Sketches for the bubble shape evolution at the different times (the unit for the indicated number is microseconds) in three stages I (compression), II (reexpansion), and III (collapsing) of B_1. (d) Time evolutions of the distances of the right edge (solid triangles), the upper edge (open circles), and the left edge of B_2 (solid squares) from the laser position. Before 15 μs, the circles and squares coincide.

tial snapshots of shadowgraphs in Fig. 3(a) show the dynamical evolution of an initially stationary bubble (B_1, right) perturbed by a second nearby bubble (B_2, left) at $E_1=220$ μJ, $E_2=90$ μJ, and $D_L=500$ μm (corresponding to case B in Table I). B_1 and B_2 are generated at $t=-10$ and 0 s respectively. Figure 4(a) depicts the time evolution of the volumes (by digitally measuring the areas of the bubbles from CCD pictures) of B_1 and B_2 in Fig. 3(a) (normalized to the initial volume of B_1). Stages I, II, and III in Fig. 4(a) represent the sequential compression, reexpansion, and the final contraction stages of B_1, respectively. In stage I, the pressure perturbation travels at about 900 m/s and reaches the left edge of B_1 in 0.5 μs (not shown). At $t=1$ μs, the pressure front supporting the strong pressure gradient has already reached the left edge of B_1 and caused its rightward deformation. Due to the 1 μs exposure time of the ICCD camera, the high-speed motion of the B_2 boundary causes a blurred image for $t=1$ μs. The instability associated with the continuous compressional perturbation leads to the formation of a rightward axial jet, while the right edge of B_1 remains unperturbed in the entire stage I (from 0.5 to 6 μs). The average velocity of the axial jet through B_1 (from the bubble indentation to the jet reaching the right edge of B_1) and the initial bubble expansion velocity of B_2 (in the initial 1 μs) are shown in Table I and Fig. 2(d), respectively. The jet (expansion) velocity increases with the laser energy used for generating B_2. Their corresponding Weber and Reynolds numbers are also shown in Table I. Since the Reynolds and Weber numbers are both large, stage I is dominated by the inertia effect. Viscosity and surface tension can both be neglected. That is, the RM instability is the origin for the formation of the rightward jet. At $t=6$ μs, the jet hits the right edge of B_1 and splits B_1 into two symmetric parts. The volume also reaches a minimum.

After the above overcompression, the reexpansion stage II begins. A butterfly-shaped pattern with two symmetric side lobes is observed associated with the deeper protrusion of the jet into the liquid beyond the right edge of B_1, where necking occurs. The necking gradually becomes less obvious and disappears in the expansion process. In stage III (after 35 μs), the two kidney-shaped lobes start to contract again, and evolve to the two final stable circular daughter bubbles under the surface tension effect. Note that the white region inside the deformed B_1 is the unwetted area [indicated by the arrow in the frame at 35 μs in Fig. 3(a)] corresponding to the minimum volume during B_1 deformation [see Fig. 3(b) at 6 μs]. The remaining region inside the reexpanding B_1 is gray. This suggests that there is a thin liquid film left on the glass surface inside B_1 when the rebounding gas pushes out most of the liquid in the gap in the reexpansion stage of B_1.

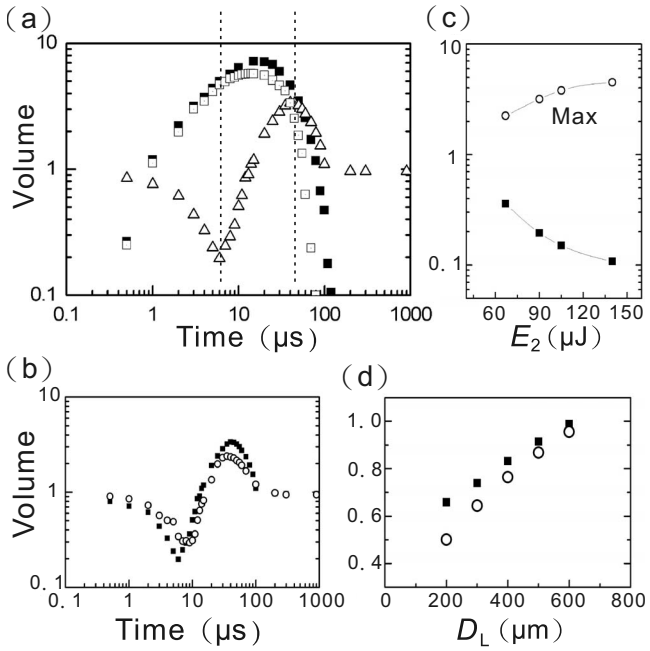

FIG. 4. (a) Temporal evolution of the volumes of B_1 (open triangles) and B_2 (open squares) for case B (E_2=90 μJ and D_L =500 μm). Stages I–III correspond to the compression, reexpansion, and final collapse stages of B_1. The solid squares show the volume evolution of B_2 under the same conditions but in the absence of B_1, which shows the larger maximum expanding volume and the slow final decay because of the lack of energy transfer to B_1. (b) Volume evolutions of B_1 at E_2 of 75 (open circles) and 90 μJ (solid squares). (c) Minimum compression (solid squares) and maximum expansion (open circles) volumes of B_1. All the volumes shown in (a)–(c) are normalized by the initial volume of B_1. (d) Ratios of the maximum expanding volumes of B_2 at the different D_L to that of the B_1-free case, at the gap width of 10 (solid squares) and 30 μm (open circles).

The lower transmission of the illuminating light due to the thin liquid film makes this region gray. This region gradually becomes whiter after the film dries up in the later stage [e.g., see the 3 ms image in Fig. 3(a)]. The axial jet has the same dark gray color as the liquids surrounding both bubbles. This indicates that the axial jet is not sandwiched by thin gas layers vertically.

From the viewpoint of the internal pressure, the bubble volume provides important information during bubble interaction. The two compressible bubbles are similar to two damped oscillators coupled by the background liquid. Energy is transferred through the expansion-compression processes. This is the key mechanism for the compression, expansion, and collapse stages for B_1. Figure 4(b) shows that increasing E_2 increases the extreme compression and reexpansion volume ratios of B_1. Figure 4(a) further shows that, in the absence of B_1, B_2 can expand to a larger volume and collapses more slowly. Figure 4(c) shows that increasing E_2 decreases (increases) the minimum (maximum) volume of B_1 at the end of stage I (II). It indicates the stronger compression and the later stronger rebound of B_1 with increasing energy of B_2.

Figure 3(b) and 3(c) show expanded pictures and sketches of the formation of the jet and the following butterfly-shaped pattern formation, respectively. The pictures of B_1 from 5 to 9 μs depict the butterfly-shaped reexpanding pattern of B_1. Similarly to the impact of a liquid column from air onto an air-liquid interface [27,28], the protrusion of the liquid jet into the right edge of B_1 is associated with some compressed high-pressure gas, which causes the formation of extended cavities near the tip of the penetrating jet after 7 μs. The interplay with the newly arrived high-pressure flow front surrounding the compressed B_1 induces the necking of the butterfly-shaped pattern through the generation of the two transverse jets. A similar butterfly-shaped pattern formation following the protrusion jet has also been observed for a collapsing bubble near the solid boundary [15].

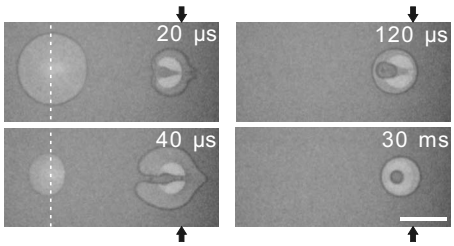

FIG. 5. Sequential snapshots of the evolution of B_1 and B_2 for case A (E_2=67 μJ and D_L=500 μm). The weak perturbation from the expanding B_2 at low E_2 generates a weak axial jet which is not strong enough to fragment B_1 but leads to the pinching of the two left boundaries of B_1 and the enclosure of a liquid droplet in B_1. The backward interaction from the expanding B_1 also makes the shape of B_2 noncircular. The vertical dashed line and the arrows indicate the initial horizontal positions of the centers of B_1 and the right edges of B_1 respectively. Scale bar 200 μm.

C. Droplet inclusion under weak impact

What will happen if the axial jet is not strong enough to split B_1? Figure 5 depicts the behavior of case A in which the strength of the impact on B_1 is weakened by decreasing E_2 to 67 μJ but at the same D_L (500 μm). A weak rightward jet is formed on B_1. B_1 reaches the minimum volume at 15 μs while the jet reaches the right edge of B_1. The strength of the impact is too weak to cause the formation of the butterfly-shaped pattern with two transverse jets. A weak axial jet only forms a nipple on the right edge of B_1, which lasts till the beginning few microseconds in stage III (the final collapsing stage of B_1). The cusp-shaped opening associated with the initial jet on the left edge of B_1 eventually pinches. It leaves a liquid droplet enclosed in B_1 (see the final pictures at 120 μs and 30 ms in Fig. 5). If the pinching does not occur, the droplet inclusion does not occur. The probability of droplet inclusion in this operation condition is shown in Fig. 10(c) below.

D. Stronger impact on increasing E_2

The strength of the impact of B_2 on B_1 can be increased by increasing E_2 or deceasing D_L. The former increases the pressure and the speed of the B_2-induced flow front, and the total duration for the expansion stage of B_2. The latter increases the initial impact and changes the curvature of the

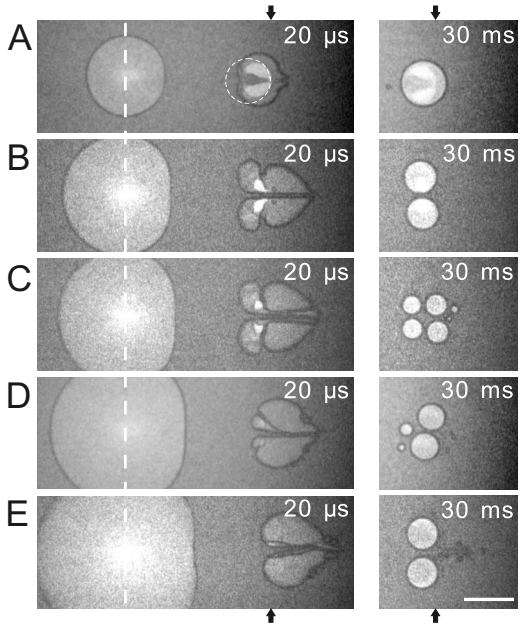

FIG. 6. Typical snapshots at 20 μs for cases A–E, showing that the increasing strength of the expanding B_2 with increasing E_2 suppresses the leftward re-expansion of B_1 and leads to the different number of final fragmented bubbles. In case C, the inward transverse jets become unstable. The vertical dashed line and the arrows indicate the initial horizontal positions of the centers of B_2 and the right edges of B_1, respectively. The dashed circle in case A corresponds to the initial boundary of B_1. Scale bar 200 μm.

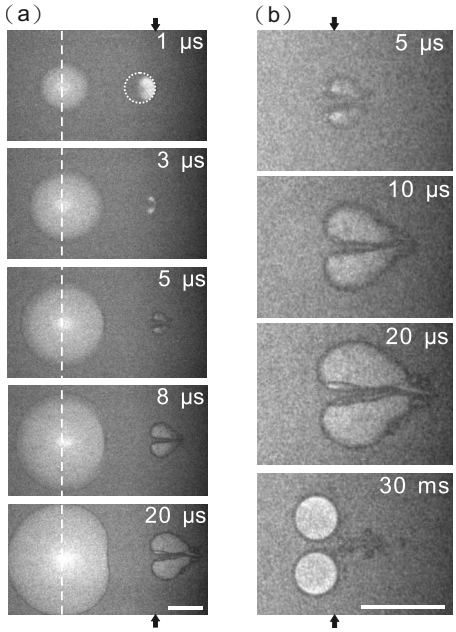

FIG. 7. (a) Snapshots showing the evolution of bubble shapes for case E (E_2=140 μJ and D_L=500 μm). The dashed circle at 1 μs corresponds to the initial boundary of B_1. (b) Expanded pictures showing the unstable boundary of B_1 under strong shear from the axial jet and the surrounding flow field, which generates many tiny final bubbles. The vertical dashed line and the arrows indicate the initial horizontal positions of the centers of B_2 and the right edges of B_1, respectively. Scale bars: 200 μm.

impact front. The transient states at 20 μs and the final states of cases A, B, C, D, and E at the same D_L (500 μm) but different E_2 (67, 90, 105, 120, and 140 μJ, respectively) are shown in Fig. 6. Comparing with case B [see the details in Fig. 3(a)], the stronger impact from B_2 in case C further shatters the two side lobes of B_1 into more daughter bubbles. However, further increasing E_2 to 140 μJ (case *E* in Fig. 7) suppresses the leftward re-expansion in stage II and leads to two major symmetric fragmented bubbles accompanied by many tiny bubbles on the right side.

Figure 8 depicts the more detailed fragmentation information of B_2 for case C. Compared to case B [see Fig. 8(a) and the pictures at 5 and 8 μs in Fig. 3(a)], the initial compression with a rightward axial jet formation on B_2 for case C is quite similar, but with a shorter time for the onset of stage II, a smaller minimum volume for compression, and a larger width of the axial jet. The stronger transverse inward jets from the necking region of the butterfly-shaped pattern play very important roles, leading to the complicated fragmentation pattern. The transverse jets from the two opposite side lobes are not always symmetric. The few shadowgraphs at 20 μs in the expansion process from the different runs with the same initial condition in Figs. 8(c)–8(f) show the different intermediate states that lead to the different final fragmentation patterns at 30 ms. That is, the transverse inward jets from the edges of the necking regions are quite unstable. They either directly merge with the rightward axial jet or bifurcate and turn outward again before hitting the rightward axial jet. These asymmetric transverse jets split the butterfly-shaped pattern into more separate pieces, with the same number as that of the final fragmented circular bubbles shown at 30 ms. Note that in a few tens of tested runs with similar and slightly smaller E_2, we have not observed any transverse jet initiating from the outer right boundary of either side lobe without reaching the axial jet. This leads to our conjecture that those transverse jets are moving transversely outward, induced by the inward transverse jets in the necking region.

Increase of E_2 from 105 μJ (case C) to 120 μJ (case D) suppresses the leftward expansion in stage II of B_1 (Fig. 6). For example, the left side lobes are very small; only the upper transverse jet from the necking region reaches the rightward axial jet and induces the final fragmentation into two larger daughter bubbles and one small bubble for case D. Unlike the intuitive expectation, further increase of E_2 to 140 μJ (see case E in Fig. 8) does not shatter the two reexpansion side lobes into many small pieces. It leaves two major symmetric large circular daughter bubbles with many tiny bubbles on their right-hand side. The strong B_2 expansion pushes B_1 rightward by fully suppressing (enhancing) the leftward (rightward) reexpanding part of B_1 in stage II after the minimum compression of B_1 at 3 μs. Therefore, no unwetted regions are observed in the reexpansion stage in case *E* (Fig. 6). The impact is strong enough to keep the axial jet and the flow surrounding B_1 exceeding the critical velocity (10 m/s) for the onset of the Kelvin-Helmholtz (KH) instability. It leads to the formation of the tiny bubbles along the boundary. For other cases at smaller E_2, even though the initial jet velocities are also higher than the threshold, the

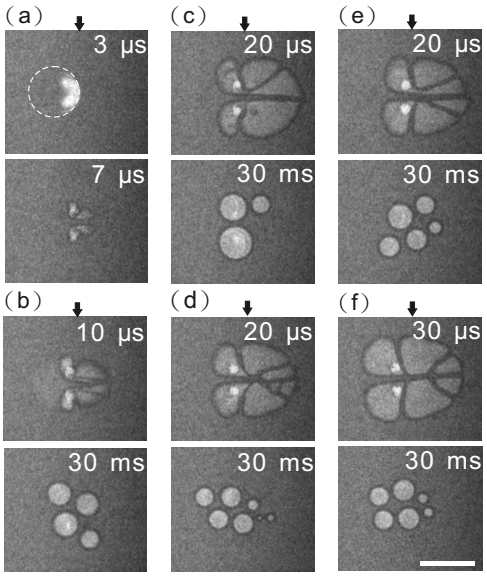

FIG. 8. Snapshots showing the evolution of the bubble shapes for case C (E_2=105 μJ and D_L=500 μm). The inward transverse jets from the neck of the side lobes of the expanding B_1 become unstable. They can directly meet with the axial rightward jet or go outward again. It not only makes the patterns of the two side lobes asymmetric in the same run, but also makes the patterns different from run to run under the same condition. (c)–(f) show the different sets of typical intermediate states for B_1 at stage II (t=20 μs) and the corresponding final states (30 ms) obtained in the same runs. The dashed circle corresponds to the initial boundary of B_1. The arrows indicate the initial right edges of B_1. Scale bar 200 μm.

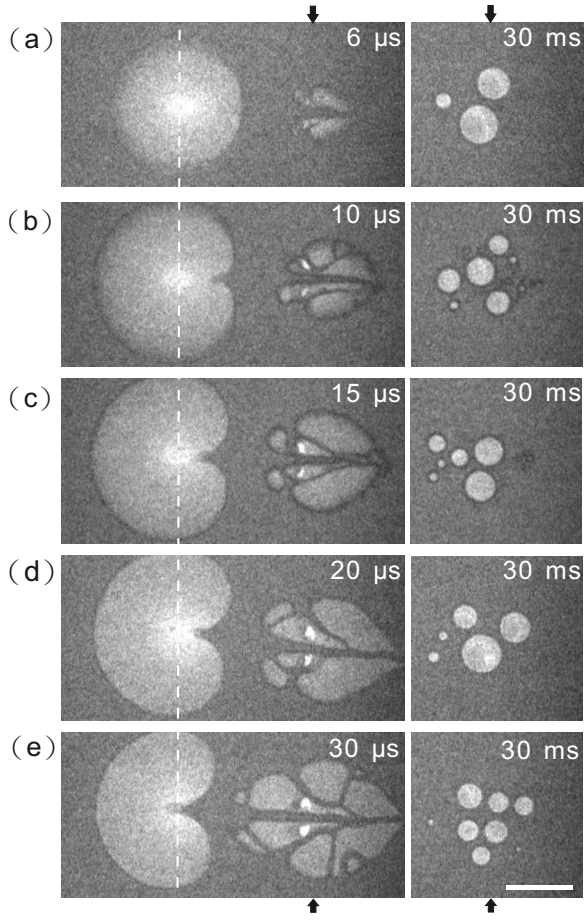

FIG. 9. A few typical sets of the complicated patterns of B_1 for the intermediate states and the corresponding final circular bubbles at 30 ms fragmented by strong unstable jets for case F (E_2 =105 μJ and D_L=350 μm). The vertical dashed line and the arrows indicate the initial horizontal positions of the center of B_2 and the right edges of B_1 respectively. Scale bar 200 μm.

fast decay of velocities associated with the collapsing B_2 is not sufficient to drive the KH instability. Also note that, for a liquid jet in a three-dimensional (3D) gas, the capillary instability leads to the pinching off of the jet. The pinching-off time scale τ for a 3D jet under the same jet diameter, liquid density, and surface tension as our jet is about 15 μs [$\tau = (r^3\rho/\gamma)^{1/2}$, where r, ρ, and γ are the jet radius, liquid density, and surface tension of the liquid jet respectively] [29]. However, in our system, the axial jet is sandwiched by two glass boundaries. Unlike the cylindrically symmetric liquid column, the undulation of the liquid-gas surface actually leads to larger surface area and in turn higher surface energy, which prevents the capillary instability (note that the contact angle for our liquid-glass interface is only 5°, which means that wetting is preferred for the liquid-gas interface).

E. Strong impact on decreasing D_L

What will happen in case F (Fig. 9), where we change E_2 back to 105 μJ (the same as in case C), but shorten D_L to 350 μm (shorter than 500 μm for case C)? Obviously, decreasing D_L increases the coupling between the two bubbles. Figure 4(d) shows the decrease of the maximum expanding volume of B_2, normalized by that in the absence of B_1, with decreasing D_L. It reflects the increasing energy transfer from B_2 to B_1 with decreasing D_L. The stronger impact under the shorter D_L shortens the duration of stage I (it ends at 3 μs; not shown), with a wider axial jet, and generates more than one transverse jet for the left reexpansion part of each side lobe (see the pictures from 10 to 30 μs in Fig. 9), which leads to quite complicated asymmetric final fragmentation patterns. As in case C, the detailed fragmentation is not reproducible because of the instabilities associated with the strong jets.

Figure 10(a) depicts the statistical results for the fragmentation numbers of cases B, C, and F. The transverse jets in cases C and F make the fragmentation patterns more complicated with higher fragmentation number than in case B. The wider distribution of fragmentation number also reflects poor reproducibility of the fragmentation pattern of the shattered B_1 from run to run. Furthermore, we measure the standard deviation of the volume of the daughter bubbles (normalized by the initial size of B_1) of B_1 from each image at 30 ms, and plot the probability distribution of the standard deviation from a few tens of images [Fig. 10(b)]. The mean deviation of bubble sizes of case F is higher than that of case C. It reflects the fact that the bifurcation of transverse jets can make the fragmentation pattern of B_1 more complicated.

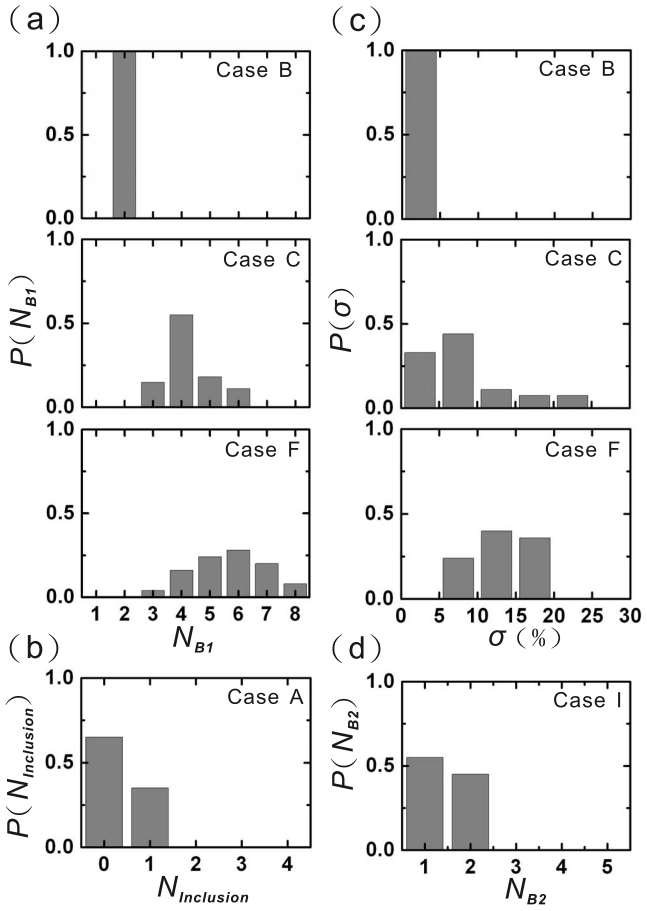

FIG. 10. (a) The histograms $P(N_{B_1})$ of the number of final fragmented daughter bubbles from B_1 for cases B, C, and F. (b) Histogram $P(N_{\text{inclusion}})$ of the number of droplet inclusions in B_1 for case A. (c) Histograms $P(\sigma)$ of the standard deviation of the volume fraction (normalized by the initial volume of B_1) of the final fragmented daughter bubbles from B_1 for cases B, C, and F. (d) Histogram $P(N_{B2})$ of the number of final fragmented daughter bubbles from B_2 for cases I.

Note that cases F (small D_L and small E_2, Fig. 9) and E (large D_L and large E_2, Fig. 7) both provide stronger impact on B_1 than in case C (large D_L and small E_2, Fig. 8). In case E, the larger E_2 makes B_2 still expand when B_1 enters stage II, which fully suppresses the leftward expansion of B_1. However, in case F, the faster collapsing of B_2 at smaller E_2 allows the leftward expansion of B_1 after the strong impact by B_2 at the shorter D_L. The leftward expansion of B_1 can be enhanced associated with the formation of a backward jet on the right edge of B_2 as it collapses. More details can be found in the next section on backward interaction.

From case F, case G further decreases E_2 to 90 μJ and D_L to 300 μm (with the same E_2 as in case B). Compared to case B, the strong initial impact at the shorter D_L makes a faster ending of stage I at 4 μs with a wider axial jet (Fig. 11). The pattern of B_1 in stage II changes from a butterfly to a bug shape (see the 9–25 μs pictures in Fig. 11). Its left-pointed head can be entrained into the collapsing B_2, and forms a squid-shaped intermediate pattern at 30 μs.

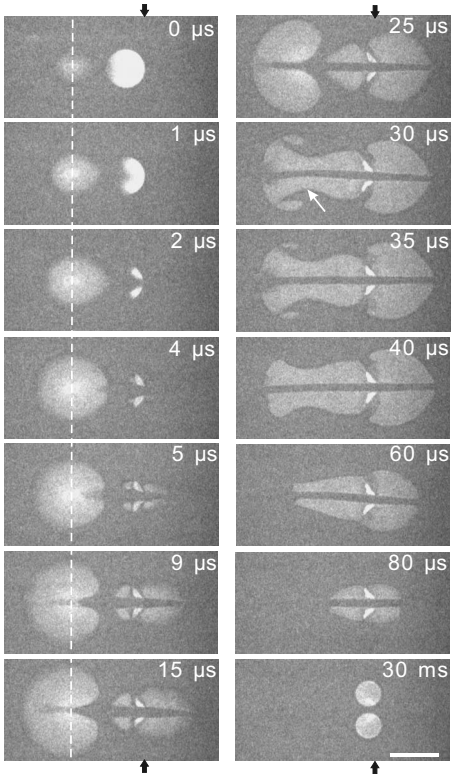

FIG. 11. Snapshots showing the bubble evolution for case G (E_2=90 μJ and D_L=300 μm). The short D_L induces a pendant-shaped elongation of B_2 with a pointed pole entrained toward the indented edge induced by the forward axial jet on B_1 (t=2 μs). The backward jet on B_2 is formed after B_2 enters stage II. It leads to a bug-shaped B_1 and the entrainment of the left edge of the expanding B_1 and the entanglement with B_2. The vertical dashed lines and the black arrows indicate the initial horizontal positions of the centers of B_2 and the right edges of B_1, respectively. The white arrow in the 30 μs panel indicates the mushroom region. Scale bar 200 μm.

F. Backward interaction I: elongation and backward jetting of B_2

The presence of B_1 with a deformable liquid-gas interface also makes the liquid background for the expanding and collapsing B_2 anisotropic. Since the pressure field from B_2 reaches B_1 within about 0.5 μs for case B, the shape of B_2 is noncircular in nearly the entire process under the backward interaction. Figure 3(d) shows the time evolution of the relative distances from the different (right, left, upper) edges of B_2 to the laser position for generating B_2. Initially, B_2 is elongated toward B_1 before 8 μs. That is, compared with the indentation of the left edge of B_1, the right edge of B_2 moves faster than the other three edges (upper, lower, and left edges). However, this trend is then reversed and the right front of B_2 is flattened with retarded rightward motion, after B_1 starts to expand (at 8 μs), no matter whether B_2 is still in its expanding phase or in the subsequent collapsing phase. Therefore, the right edge of B_2 reaches the maximum distance earlier than the other two edges [see the crossover of the curves at 8 μs in Fig. 3(d)]. Note that the square (the left edge location with respect to the laser position) and the circle

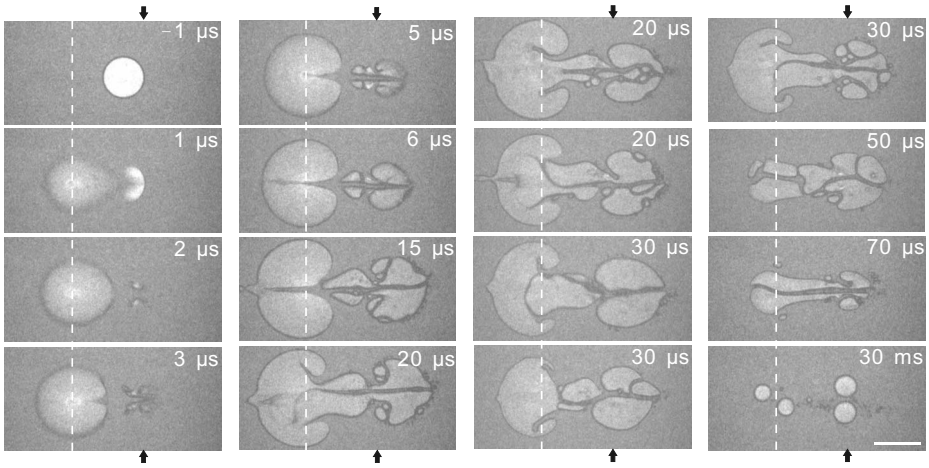

FIG. 12. Snapshots showing the bubble shape evolution for case H (E_2=90 μJ and D_L=225 μm). The stronger bubble coupling and earlier collapse of B_2 at the shorter D_L and the smaller E_2 than in case F induces stronger push-pull jetting and entrainment and leads to more complicated entanglement between the two bubbles. The few intermediate snapshots (20 and 30 ms) show the unstable entanglement patterns taken from different runs under the same initial conditions. The vertical dashed line and the arrows indicate the initial horizontal positions of the center of B_2 and the right edge of B_1 respectively. Scale bar 200 μm.

(the upper edge location) data coincide initially and then deviate after 15 μs, as shown in Fig. 3(d). That is, the leftward perturbation from the reexpanding B_1 starts to make the left half boundary of B_2 slightly noncircular after 15 μs. Similar flattening of the right edge of B_2 can be observed from cases A to E (see Fig. 6), where their D_L are all kept at 500 μm.

At the shorter D_L (300 μm in case G), the deformations on B_2 are further amplified due to the stronger coupling between B_1 and B_2. The further elongation at stage I causes a pendant-shaped expanding B_2 with the pointed pole toward the indented left edge of B_1 (see the 2 μs picture of Fig. 11). However, at 4 μs, a backward jet starts to form on the right edge of the still expanding B_2. This jet keeps growing leftward, accompanied by the leftward motion of the entire left boundary of B_1, while B_2 is still in its expansion mode (see the 4, 5, and 9 μs pictures in Fig. 11). That is, the perturbation from the reexpanding B_1 only reaches the right boundary of B_2 but not the other boundary. The backward jet is not strong enough to fully penetrate the left edge of B_2 up to 15 μs. Interestingly, the backward jet is also associated with the elongation of the expanding B_1 with pointed poles toward the indented right side of B_2 (see the 25 μs picture of Fig. 11), which is the main cause for the formation of the bug-shaped pattern of B_1.

The above push-pull-type motion of the two bubbles can be understood using the following simple picture. The two bubbles are like two damped oscillators coupled through hydrodynamic interaction. The potential energy can be stored in the compressed gas for each bubble. When B_2 expands, the energy can be transferred to B_1 through the compressed flow field. The interplay with inertia causes the overcompression and the subsequent rebounding of B_1. In stage I, when the pressure front reaches the left edge of B_1, the induced rightward jet causes an easier rightward flow between B_1 and B_2. It thereby induces a faster rightward expansion edge of B_2. This situation is reversed when B_1 starts to rebound. The induced leftward flow retards the expanding right edge of B_2. It not only flattens the right edge but also induces a leftward jet. Now the easier leftward flow between the two bubbles causes a faster leftward motion of the left expanding front than of the remaining boundaries of B_1, and induces the subsequent elongation or even entrainment of the pointed left pole of B_1 into the indented region of B_2. This situation is somewhat similar to the alternate jetting and entrainment behavior of an expanding and then collapsing bubble near a free surface (liquid-gas interface), e.g., in an underwater explosion [19,20]. In the bubble expansion stage, the easier water displacement in the region between the bubble and the free surface induces RM instability with a jet on the free surface (into the gas side) and an elongated bubble entrained in the indented region by the jet. The situation is reversed with backward jetting and entrainment into the bubble when the bubble collapses.

G. Backward interaction II: Entanglement between B_1 and B_2

With the above picture, the subsequent entanglement between the two closely separated bubbles in stages II and III can be easily understood. For example, the leftward flow associated with the backward jet can suck the entire leftward expanding front of B_1 into B_2 and induce a squid-shaped entangled pattern between B_1 and B_2 for case G (see the 30 μs picture of case G in Fig. 11). As the left expanding nose of B_1 coalesces with the right collapsing boundary of B_2, the thin leftward moving liquid layer between the two bubbles driven by the higher pressure of B_1 becomes unstable. In addition to the backward axial jetting on B_2, there are two backward jets on the collapsing side lobes of B_2. A mushroom-type structure (as indicated by the arrow in the 30 μs panel in Fig. 11) is thereby formed. In case H, D_L is further shorten from 300 μm in case G to 225 μm. The formation of the pendant-shaped B_2 and its strong entrain-

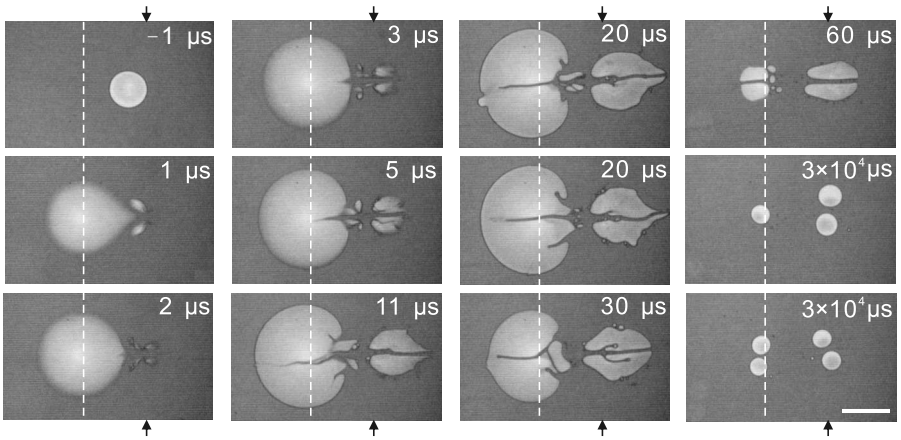

FIG. 13. Snapshots showing the bubble shape evolution for case Ie (D_L=170 μm and E_2=90 μJ). The vertical dashd line and the arrows indicate the initial horizontal positions of the centers of B_2 and the right edges of B_1, respectively. The strong merging of the left part of the reexpanding B_1 accompanied by the breaking of the necking region of B_1 leads to early entanglement termination at 6 μs. The two snapshots at 20 μs show the unstable patterns from different runs under the same initial conditions. If the leftward jet is not strong enough to penetrate B_2, only one major daughter bubbles is left at the end. Scale bar 200 μm.

ment into the indented left boundary of B_1 occur at 1 μs (Fig. 12). In stage II, the stronger coupling makes the flow and pattern between the two bubbles highly unstable. The several 20 μs pictures in Fig. 12 show the different entangled patterns obtained from different runs but with the identical initial conditions. Note that, in case G B_2 is fully sucked into B_1 in stage III. Finally, only two symmetric fragmented bubbles are left at the initial position of B_1. However, in case H, the shorter D_L makes the onset of entanglement between B_1 and B_2 happen while B_2 is still expanding, which is earlier than in case G, where the onset happens after B_2 starts to collapse. Therefore more gas and energy are pumped into the left part of the entangled pattern. The neck of the entangled pattern is then broken, which leaves two final fragmented small bubbles around the initial position of B_2, in addition to the two larger final fragmented bubbles around the initial position of B_1. Note that the sizes of the two right daughter bubbles in case H are smaller than those in case G, which reflects the loss of the total energy of B_1 to B_2 through the entanglement. Also note that, even at the short D_L for case H, the leftward jet still cannot fully penetrate B_2 and separate it into two pieces. Similarly to the weak rightward jet on B_1 for case A, the weak jet only induces a nipple at the left edge of B_2, which finally disappear in stage III (see the 15, 20, and 70 μs pictures in Fig. 12).

In case I, we further push D_L down to 170 μm and keep E_2 the same as for cases G and H to test the short-distance interaction. As shown in Fig. 13, the initial rightward entrainment of B_2 into the jet-indented surface of B_1 and the transverse necking are similar to those of cases G and H. However, the shorter D_L leads to the merging of the left part of the reexpanding B_1 accompanied by the breaking of the necking region of B_1 and in turn causes the early entanglement termination at 5 μs. Similarly to case H, the stronger interaction makes the shape of the merging region highly unstable (see the irreproducible irregular patterns obtained from different runs at 20 μs in Fig. 13), associated with one to a few leftward jets. It also breaks the axial reflection symmetry of the pattern. The insufficient liquid supply between B_1 and B_2 under small D_L also makes the leftward axial jets sometimes insufficient to fully penetrate and split B_2. It leaves one or sometimes two daughter bubbles of B_2 at the end [see the probability distribution of the fragmentation number of B_2 in Fig. 10(d)]. The leftward jets are thin and not straight.

In case J (Fig. 14) we increase E_2 to 220 μJ but relax D_L to 225 μm. Again, a pendant-shaped B_2 with pointed head entrainment into the jet-indented region on B_1, followed by backward axial jetting on B_2 is observed. Certainly, the short D_L is the key for the above processes. However, unlike in cases F–I at small E_2, the left part of the reexpanding B_1 is shattered into many tiny bubbles (see the 1 and 5 μs magnified pictures in Fig. 14). The shattering could be induced by multiple reflection of the flow field between B_1 and B_2 under large E_2 and small D_L. Similarly to case E in Fig. 8, the strong impact on B_1 also makes its right outer boundary and the central axial jet region highly unstable, associated with formation of many tiny bubbles (see the pictures from 5 to 15 μs in Fig. 14). Note again, similarly to case E, that the large E_2 makes the volume of B_2 still expand even in the expanding phase of B_1. The backward jet on B_2 is not strong enough to fully penetrate B_2. B_1 and B_2 are quickly disentangled (see the picture at 8 μs in Fig. 14), and all the tiny bubbles are pushed to the right-hand side of B_2 accompanied by the two major fragmented daughter bubbles from B_1 (see the pictures in the right column of Fig. 14). The final fragmentation bubbles of B_1 are quite similar to those in case E.

IV. CONCLUSION

We have investigated the dynamical evolution of an existing stable bubble B_1 impacted by a nearby expanding bubble B_2 induced by a pulsed laser beam in a thin liquid layer. Our system has the advantage of highly reproducible control of the initial conditions.

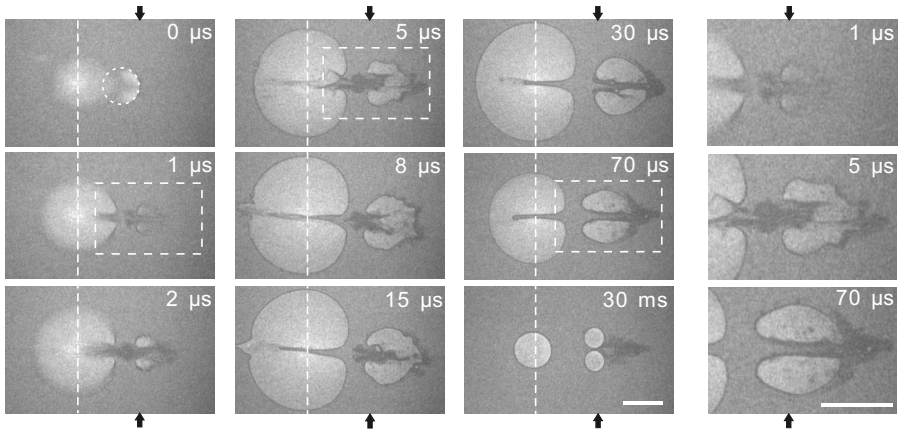

FIG. 14. Snapshots showing the bubble shape evolution for case J at the extreme of small D_L (225 μm) and large E_2 (220 μJ). The high pressure between the two bubbles under the strong interaction at the initial 3 μs generates two opposite jets and many tiny bubbles between B_1 and B_2. The still expanding right front of B_2 prevents B_2 from sucking back and entangling with B_2. It leaves the two major daughter bubbles of B_1. The tiny bubbles are pushed by the rightward flow to the left of the two daughter bubbles. The snapshots in the rightmost column are the magnified pictures from the images at 1, 5, and 70 μs. The dashed circle at 1 μs corresponds to the initial boundary of B_1. The vertical dashed line and the arrows indicate the initial horizontal positions of the centers of B_2 and the right edges of B_1 respectively. Scale bar 200 μm.

The two bubbles are similar to two coupled and damped oscillators. The potential energy can be stored through compression and transferred back and forth, mediated by the associated flow field driven by the expansion. Similarly to the jet formation associated with the anisotropic evolution of bubbles near a solid wall [13–16] or liquid-gas interface [19,20], or driven by shock waves [23], the existence of the nearby bubble and the associated flow field breaks the symmetry. The inertia-dominated RM instability plays the key role for the push-pull-type alternate jetting on the compressed bubble boundaries by a high-pressure flow field. It leads to the elongation or even entrainment of the expanding bubble into the jet-indented region of the counterbubble. Their further interplay with the flow field surrounding B_1 induces complicated fragmentation patterns of B_1. Increasing E_2 increases the strength of the impact on B_2 which not only enhances the forward jet but also induces instabilities on the entire liquid-gas boundary of B_1. Decreasing D_L enhances the push-pull-type alternate jetting and induces complicated entanglement between the two bubbles through increasing mutual interaction.

At a few hundred micrometers interbubble distance, the high-pressure front quickly reaches the left edge of B_1 in less than 1 μs. It anisotropically compresses B_1, associated with the formation of the forward axial jet. For B_2, similarly to the expansion of a bubble near a liquid-gas interface [19,20], the easier rightward displacement of the flow field elongates B_2 and forms a pendant-shaped bubble with a pointed right end which could be entrained into the indented left region of B_1 by the axial jet if D_L is short enough. After the overcompression, B_1 enters the reexpansion stage II. The expansion of B_1 again is anisotropic. The induced leftward flow field retards the rightward motion of the right boundary of B_2. Other boundaries far away from B_1 are not perturbed by this field and still maintain their circular shape in the expansion or even the initial contraction stage of B_2. A backward jet can be formed on B_2 which leads to the entrainment of the left expanding front of B_1 in the jet-indented region of B_2, if D_L is short enough and B_1 has accumulated sufficient compression energy in stage I.

In stage II, the interplay of the protrusion of the gas with the penetrating jet on B_1 and the strong B_2-induced flow field around B_1 causes the formation of butterfly-shaped patterns with two transverse jets from the neck regions on both side lobes. These two jets become unstable and are able to shatter B_1 into several daughter bubbles when E_2 increases. However, further increasing E_2 fully suppresses the leftward expansion of B_1. The absence of the two transverse jets leaves two major fragmented bubbles. The instability caused by the strong shear of the axial jet or the flow surrounding the outer boundary of B_1 generates many tiny bubbles. On the contrary, at the small-E_2 limit, the rightward axial jet is too weak to reach the right boundary of B_1. The pinching of the left edges leaves a droplet inclusion in B_1 in stage III. The mutual interaction could also be enhanced by decreasing D_L at small E_2. The strong initial compression on B_1 also leads to a complicated fragmented pattern of B_1 caused by the multiple transverse jets. However, the quick collapse of B_2 following its short expansion period allows the strong rebound of B_1, accompanied by a strong backward jet on B_2. It sucks B_1 into B_2 and leads to the complicated squid-shaped entangled pattern with a mushroom-type head on the left-hand side. Further shortening D_L at the same E_2 leads to the stronger leftward merging of the left part of the rebounding B_1 into the indented right region of B_2, which breaks the transverse necking region of B_1 and causes the earlier termination of the entanglement between the two bubbles. The insufficient liquid supply at small D_L also weakens the backward jetting. If we push to the limit of large strength of the impact at small D_L and large E_2, the strong compression and the short distance cause the pointed pole of the expanding B_2 to be fully sucked into the axial jet-indented region of B_1 in

stage I. However, the subsequent strong rebound of B_1 in stage II makes its left part shatter into many tiny bubbles entrained in the indented region by the backward jet on B_2. The quick strong rebound from B_2 suppresses the entanglement between B_1 and B_2, and pushes all the tiny bubbles to the right-hand side of the two major daughters of B_1.

ACKNOWLEDGMENTS

This work was supported by the National Science Council of the Republic of China under Contract No. NSC95-2112-M008-005.

[1] C. E. Brennen, *Cavitation and Bubble dynamics* (Oxford University Press, New York, 1995).
[2] M. Arora, C. D. Ohl, and K. A. Morch, Phys. Rev. Lett. **92**, 174501 (2004).
[3] C. D. Ohl, Phys. Fluids **14**, 3512 (2002).
[4] A. Vogel, S. Busch, and U. Parlitz, J. Acoust. Soc. Am. **100**, 148 (1996).
[5] V. Venugopalan, A. Guerra, K. Nahen, and A. Vogel, Phys. Rev. Lett. **88**, 078103 (2002).
[6] C. D. Ohl, O. Lindau, and W. Lauterborn, Phys. Rev. Lett. **80**, 393 (1998).
[7] O. Baghdassarian, H. C. Chu, B. Tabbert, and G. A. Williams, Phys. Rev. Lett. **86**, 4934 (2001).
[8] R. Pecha and B. Gompf, Phys. Rev. Lett. **84**, 1328 (2000).
[9] V. E. Dontsov and P. G. Markov, J. Appl. Mech. Tech. Phys. **32**, 41 (1991).
[10] M. Versluis, B. Schmitz, A. von der Heydt, and D. Lohse, Science **289**, 2114 (2000).
[11] D. Lohse Barbara Schmitz, and M. Versluis, Nature (London) **413**, 477 (2001).
[12] K. R. Rau, A. Guerra, A. Vogel, and V. Venugopalan, Appl. Phys. Lett. **84**, 2940 (2004).
[13] Y. Tomita and T. Kodama, J. Appl. Phys. **94**, 2809 (2003).
[14] G. N. Sankin and P. Zhong, Phys. Rev. E **74**, 046304 (2006).
[15] E. A. Brujan, G. S. Keen, A. Vogel, and J. R. Blake, Phys. Fluids **14**, 85 (2002).
[16] E. Zwaan, S. Le Gac, K. Tsuji, and C. D. Ohl, Phys. Rev. Lett. **98**, 254501 (2007).
[17] R. Richtmyer, Commun. Pure Appl. Math. **13**, 297 (1960); E. Meshkov, Fluid Dyn. **4**, 101 (1972); G. Jourdan and L. Houas, Phys. Fluids **8**, 1353 (1996).
[18] S. I. Sohn, Phys. Rev. E **69**, 036703 (2004).
[19] P. B. Robinson, J. R. Blake, T. Kodama, A. Shima, and Y. Tomita, J. Appl. Phys. **89**, 8225 (2001).
[20] A. Pearson, E. Cox, J. R. Blake, and S. R. Otto, Eng. Anal. Boundary Elem. **28**, 295 (2004).
[21] D. Ranjan, M. Anderson, J. Oakley, and R. Bonazza, Phys. Rev. Lett. **94**, 184507 (2005).
[22] C. D. Ohl and R. Ikink, Phys. Rev. Lett. **90**, 214502 (2003).
[23] G. Layes, G. Jourdan, and L. Houas, Phys. Rev. Lett. **91**, 174502 (2003).
[24] A. Tufaile and J. C. Sartorelli, Phys. Rev. E **66**, 056204 (2002).
[25] M.S. Plesset and R.B. Chapman, J. Fluid Mech. **47**, 283 (1971).
[26] Y. H. Chen, H. Y. Chu, and I. Lin, Phys. Rev. Lett. **96**, 034505 (2006).
[27] B. Kersten, C. D. Ohl, and A. Prosperetti, Phys. Fluids **15**, 821 (2003).
[28] C. D. Ohl, H. N. Oguz, and A. Prosperetti, Phys. Fluids **12**, 1710 (2000).
[29] J. Eggers, Rev. Mod. Phys. **69**, 865 (1997).